Classical sudden model for vibrational and rotational excitations in ion-molecule collisions

Atsushi Ichimura[1,*] and Masato Nakamura[2,†]
[1]*Institute of Space and Astronautical Science, Sagamihara 229-8510, Japan*
[2]*College of Science and Technology, Nihon University, Funabashi 274-8501, Japan*
(Received 25 August 2003; revised manuscript received 12 November 2003; published 26 February 2004)

We develop a classical model of an ideally sudden character for vibrational and rotational excitations in collisions of an atom (or an ion) with a diatomic molecule at energies as high as $10–10^2$ eV. The energy-loss spectra with vibrotational levels left unresolved are analytically expressed with a repulsive intermolecular potential in a *hard potential* limit (i.e., a vanishing range of force). It turns out to be an extension of the *hard shell* model for a rigid-rotor molecule developed by Beck *et al.* two decades ago. For a homonuclear molecule, the hard potential model generally derives spectra with double peaks at both edges, one nearly elastic and another deeply inelastic. They are analogous to rotational rainbows though their positions are affected by vibrational excitation. Classical trajectory calculations with a finite-range model potential are carried out for collision systems of $H^+ + N_2$ and $Li^+ + N_2$, and systematically compared with the model. It is found that the effect of vibrational excitation manifests itself the way the model predicts. It is also demonstrated that the spectra are virtually reduced to the hard potential model when the vibrational period is artificially taken much longer than a collision time, while reduced to the hard shell model when much shorter.

DOI: 10.1103/PhysRevA.69.022716 PACS number(s): 34.10.+x, 34.50.Ez

I. INTRODUCTION

Certain aspects of vibrational and rotational excitations in collisions of an atom (or an ion) with a diatomic molecule are dominated by a short-range repulsive intermolecular force [1–5]. Since the force range λ is much shorter than a molecular size [6], the molecule looks as a hard-wall ellipsoid, on which an instantaneous torque would excite high rotational states $j \gg 1$ nonperturbatively. On this basis, a classical *hard shell* (or *rigid shell)* model was developed by Beck *et al.* [7] two decades ago. Because of its simplicity, the model and its variations have been widely applied to collisions at hyperthermal energies such as $10^{-1}–1$ eV (equivalent velocities of $v \sim 10^{-3}$ a.u.) [8–19]. They reveal universal emergence of a gross peak structure called *rotational rainbow* in the j distributions at large scattering angles [3–5]. The hard shell model is valid when a collision is *sudden* with respect to rotational motion [10,15], i.e., when the collision time $\tau \sim \lambda/v$ with velocity v is much shorter than a rotational period while longer than a vibrational period. In fact, vibrationally elastic scatterings are dominantly observed, and occasionally low discrete vibrational transitions are also noticeable [20]. The rotational rainbow structure appears in the j distribution for respective vibrational levels n.

Some experiments have been done, however, at much higher energies such as $10–10^2$ eV (equivalent velocities of $v \sim 10^{-2}$ a.u.), where the energy-loss spectra have been measured in electronically elastic scatterings, leaving individual vibrotational levels (n,j) unresolved [21–23]. Among them, collisions of $Li^+ + N_2$ have been investigated over a wide range of the center-of-mass energies as $E = 4–17$ eV [20,21] and $E = 60–300$ eV [22]. Throughout these energies, the energy-loss spectra persistently exhibit two widely spaced maxima, i.e., one broad nearly elastic peak and one broad deeply inelastic peak. Although emergence of the double-peak structures is consistent with rotational rainbow, no systematic interpretation has been given all through the observations. In particular, effects of vibrational excitation seem still unclear, though some analyses have been carried out with classical trajectory calculations [20,21] and with more sophisticated semiclassical calculations [24,25].

In such energies, the collision could be sudden even with respect to vibrational motion, substantially exciting high vibrational $n \gg 1$, as well as high rotational $j \gg 1$, states. The higher the energy increases, the more clearly the sudden character should appear, because the repulsive force plays more dominantly, and also because even a small fraction (say, $\sim 10\%$) of available energy ($\propto v^2$) well exceeds a quantum perturbation energy ($\propto \tau^{-1} \propto v$) according to Massey's criterion. Thus arise questions whether and how the sudden character with respect to *both* vibrational *and* rotational motions actually manifests itself in the energy-loss spectra.

In the present paper, we develop a model of an ideally sudden character to elucidate the problem above. The model, called *hard potential model*, is formulated in classical mechanics by taking a limit $\lambda \to 0$ of vanishing range of force, which permits us to derive an analytic expression for energy-loss spectra. This treatment turns out to be a natural extension of the *hard shell model* [7,11], incorporating the freedoms of vibrational and rotational motions in a unified manner. We apply the model to a homonuclear molecule, and predict spectra with double peaks at both edges, whose positions are affected by vibrational excitation. We also carry out classical trajectory (CT) calculations with a finite-range model potential for $H^+ + N_2$ and $Li^+ + N_2$ collisions. The spectra obtained are systematically compared with the model, and examined for emergence of double peaks along with their dependences on the scattering angle and the re-

*Email address: ichimura@pub.isas.ac.jp
†Email address: mooming@phys.ge.cst.nihon-u.ac.jp

duced mass. Manifestations of the sudden character are also demonstrated by artificially modifying the vibrational period.

In the following section, we formulate the hard potential model and analytically express the energy-loss spectra. In Sec. III, an overall spectral profile is generally derived for a homonuclear molecule. In Sec. IV, the CT calculations are carried out and systematically compared with the model. Concluding remarks are given in Sec. V.

II. FORMULATION OF THE HARD POTENTIAL MODEL

We consider collisions of an atom (or ion) A with a diatomic molecule BC. The Hamiltonian in the center-of-mass frame reads

$$H(\boldsymbol{p},\boldsymbol{P},\boldsymbol{r},\boldsymbol{R})=\frac{\boldsymbol{p}^2}{2m}+\frac{\boldsymbol{P}^2}{2M}+U(R)+V(\boldsymbol{r},\boldsymbol{R}), \tag{1}$$

where the relative coordinates and their conjugate momenta are denoted by $\boldsymbol{r}$ and $\boldsymbol{p}$ between A and BC, and by $\boldsymbol{R}$ and $\boldsymbol{P}$ between B and C, their reduced masses being m and M. Electronically adiabatic interaction is given by a sum of the intermolecular and intramolecular potentials $V(\boldsymbol{r},\boldsymbol{R})$ and $U(R)$. The molecule is assumed to be initially neither vibrating nor rotating ($\boldsymbol{P}_{\mathrm{i}}=\boldsymbol{0}$) at an equilibrium distance R_{eq} where $\partial U/\partial \boldsymbol{R}=0$. Thus, the initial conditions are specified by three vectors: incident velocity $\boldsymbol{v}$, impact parameter $\boldsymbol{b}$ satisfying $\boldsymbol{b}\cdot\boldsymbol{v}=0$, and initial orientation $\hat{\boldsymbol{a}}$ of the molecular axis.

If all the trajectories are solved, any scalar observable ξ in the final state can be expressed as a function of initial variables as $\xi=\xi^*(\boldsymbol{v},\boldsymbol{b},\hat{\boldsymbol{a}})$. Hence, a cross section differentiated over ξ is given as

$$\sigma_\xi=\int d\sigma\,\delta(\xi-\xi^*(\boldsymbol{v},\boldsymbol{b},\hat{\boldsymbol{a}})), \tag{2}$$

with a cross-section element

$$d\sigma=\frac{1}{4\pi}d^2\hat{\boldsymbol{v}}\,d^2\boldsymbol{b}, \tag{3}$$

when molecules are randomly oriented. In this form, the cross section is obtained for, and independent of, a fixed $\hat{\boldsymbol{a}}$.

A. Impulse in the hard potential limit

For a trajectory of large deflection, momentum transfer is dominantly given in a narrow region close to the equipotential surface $\mathcal{S}_E$ at an energy $E=m\boldsymbol{v}^2/2$. In this region, we introduce local curvilinear coordinates s, s_1, and s_2 for intermolecular position $\boldsymbol{r}$ in a body-fixed frame; s represents a path length from the surface $\mathcal{S}_E$ along the force field $-\partial V/\partial\mathbf{r}$, while s_1 and s_2 span the surface (see Fig. 1). Thus, expanding $\ln(V/E)$ over s around $s=0$ up to the first-order term, we obtain

$$V(\boldsymbol{r},\boldsymbol{R})\simeq E\exp\left(-\frac{s}{\lambda}\right), \tag{4}$$

with a range parameter $\lambda(s_1,s_2,\boldsymbol{R})$.

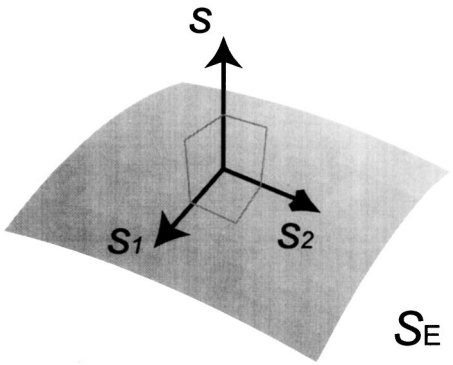

FIG. 1. Curvilinear coordinates s, s_1, and s_2, referring to the equipotential surface $\mathcal{S}_E$.

We take the limit $\lambda\to 0$ of hard potential. The force derived from Eq. (4) is exerted only when $s>0$ and $s=O(\lambda)$, so that the differential of s/λ is estimated as $\lambda d(s/\lambda)=ds-(s/\lambda)d\lambda\simeq ds$, where $d\lambda\simeq O(\lambda)$ though still $ds\simeq O(1)$. Hence, an instantaneous but finite impulse is obtained in a form of $(\delta\boldsymbol{p},\delta\boldsymbol{P})\simeq c(\partial s/\partial\boldsymbol{r},\partial s/\partial\boldsymbol{R})_{s=0}$, where a proportional constant c is determined without actually solving trajectories but by using the energy conservation (see Ref. [26]), i.e.,

$$\begin{pmatrix}\delta\boldsymbol{p}\\ \delta\boldsymbol{P}\end{pmatrix}=-2\left[\frac{m\boldsymbol{v}\cdot(\partial s/\partial\boldsymbol{r})}{1+(m/M)(\partial s/\partial\boldsymbol{R})^2}\begin{pmatrix}\partial s/\partial\boldsymbol{r}\\ \partial s/\partial\boldsymbol{R}\end{pmatrix}\right]_{s=0}, \tag{5}$$

with two vectors $\partial s/\partial\boldsymbol{r}$ and $\partial s/\partial\boldsymbol{R}$ on the surface $\mathcal{S}_E$. In the impulse (5), the intramolecular force $-\partial U/\partial\boldsymbol{R}$ is ignored because it vanishes as far as the initial distance $R=R_{\mathrm{eq}}$ is retained, and also because the collision is instantaneous (see Ref. [27]).

We suppose that three-dimensional intermolecular momentum $\boldsymbol{p}_{\mathrm{f}}=m\boldsymbol{v}+\delta\boldsymbol{p}$ is measured in the final state to determine the scaled energy-loss $\epsilon=1-\boldsymbol{p}_{\mathrm{f}}^2/(2mE)$ and the scattering angle $\cos\theta=\hat{\boldsymbol{p}}_{\mathrm{f}}\cdot\hat{\boldsymbol{v}}$. They are expressed through Eq. (5) as

$$\epsilon=\frac{4q}{(1+q)^2}\cos^2\alpha, \tag{6}$$

$$\cos\theta=\frac{q-\cos 2\alpha}{\sqrt{1+q^2-2q\cos 2\alpha}}, \tag{7}$$

with two nondimensional scalar functions defined on the surface $\mathcal{S}_E$,

$$q(s_1,s_2)=\frac{m}{M}\left[\frac{\partial s}{\partial\boldsymbol{R}}\right]_{s=0}^2, \tag{8}$$

$$\cos\alpha(s_1,s_2)=-\hat{\boldsymbol{v}}\cdot\left.\frac{\partial s}{\partial\boldsymbol{r}}\right|_{s=0}, \tag{9}$$

where a contact point (s_1,s_2) is uniquely determined by initial conditions of the trajectory. The function α in Eq. (9)

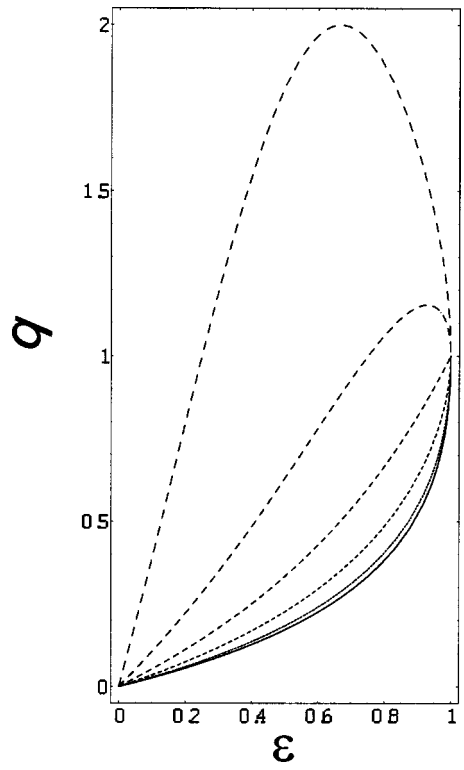

FIG. 2. The function $q^*(\epsilon;\cos\theta)$ defined in Eq. (10). The solid line represents the functions with $\theta=\pi$, while the dashed lines with $\theta=\pi/6$, $\pi/3$, $\pi/2$, $2\pi/3$, and $5\pi/6$, where the longer the dash, the smaller the θ.

represents *zenith angle* of incidence, varying in a range of $0\leqslant\alpha\leqslant\pi/2$. The function q $(\geqslant 0)$ in Eq. (8) represents *inelasticity* of the surface $\mathcal{S}_E$. If $q=0$, it behaves as a fixed *hard wall*, on which only elastic reflection occurs as $\epsilon=0$ and $\theta=\pi-2\alpha$. Combining Eqs. (6) and (7), we obtain a relation

$$q(s_1,s_2)=\frac{\epsilon}{(\sqrt{1-\epsilon}-\cos\theta)^2+\sin^2\theta}\equiv q^*(\epsilon;\cos\theta). \tag{10}$$

As far as the range of $q(s_1,s_2)$ is within $0\leqslant q\leqslant 1$, this equation gives one-to-one correspondence between energy loss ϵ and inelasticity q (see Fig. 2), hence solved as

$$\epsilon=\frac{2q}{(1+q)^2}[1+q\sin^2\theta-\cos\theta\sqrt{1-q^2\sin^2\theta}]$$
$$\equiv\epsilon^*(q;\cos\theta). \tag{11}$$

B. Integrals over inelasticity q on the surface

In the hard potential limit, since the integral element $d^2\boldsymbol{b}$ is converted to an area element dS on a convex surface $\mathcal{S}_E$, the cross-section element (3) is reduced to $d\sigma=(1/2)\cos\alpha\sin\alpha d\alpha dS$. Hence, any cross section (2) is expressed as

$$\sigma_\xi=\int_0^1 dq\frac{dS}{dq}F_\xi(q), \tag{12}$$

with

$$F_\xi(q)=\left(\frac{dS}{dq}\right)^{-1}\int d\sigma\delta(\xi-\xi^*(\boldsymbol{v},\boldsymbol{b},\hat{\boldsymbol{a}}))\delta(q-q(s_1,s_2)),$$

where dS/dq represents a weight factor over inelasticity q, independent of observable ξ. Differential cross section is given by setting $\xi=\cos\theta$ in Eq. (12) as

$$\frac{d\sigma}{d\Omega}=\frac{1}{16\pi}\int_0^\infty dq\frac{dS}{dq}\left[\frac{1+q^2(\cos^2\theta-\sin^2\theta)}{\sqrt{1-q^2\sin^2\theta}}+2q\cos\theta\right]$$
$$\times\vartheta(q^*_{\max}(\theta)-q), \tag{13}$$

where $\vartheta(x)=0$ for $x<0$ and $\vartheta(x)=1$ for $x>0$, while $q^*_{\max}(\theta)=1$ for $\pi/2\leqslant\theta\leqslant\pi$ and $q^*_{\max}(\theta)=1/\sin\theta$ for $0\leqslant\theta<\pi/2$. Double-differential cross section is expressed by setting $\xi=\epsilon\otimes\cos\theta$ in Eq. (12) as

$$\frac{d\sigma}{d\epsilon\,d\Omega}=\frac{\sqrt{1-\epsilon}}{16\pi\epsilon}\left[q(1+q)^2\frac{dS}{dq}\right]_{q=q^*(\epsilon;\cos\theta)}. \tag{14}$$

This is proportional to the weight factor dS/dq itself at $q=q^*(\epsilon;\cos\theta)$ in Eq. (10).

The domain of energy-loss in Eq. (14) is given from the range $[q_{\min},q_{\max}]$ of inelasticity $q(s_1,s_2)$ through $\epsilon^*(q;\cos\theta)$ in Eq. (11). When convoluted with a finite resolution $\Delta\epsilon$, the energy-loss spectrum (14) is transformed into

$$\left\langle\frac{d\sigma}{d\epsilon\,d\Omega}\right\rangle_{\Delta\epsilon}=\int_0^1 d\epsilon^*\frac{d\sigma}{d\epsilon^*d\Omega}I_{\Delta\epsilon}(\epsilon^*-\epsilon)=\int_0^1 dq\frac{dS}{dq}\left[\frac{(1+q)^2(1-\epsilon^*)I_{\Delta\epsilon}(\epsilon^*-\epsilon)}{16\pi|(1+q)\sqrt{1-\epsilon^*}-q\cos\theta|}\right]_{\epsilon^*=\epsilon^*(q;\cos\theta)}, \tag{15}$$

where $I_{\Delta\epsilon}$ denotes an instrumental function normalized as $\int d\epsilon^* I_{\Delta\epsilon}(\epsilon^*-\epsilon)=1$. The expression (15) still satisfies the form of Eq. (12). When $q_{\max}\ll 1$, Eq. (15) combined with Eq. (11) is reduced to

$$\left\langle\frac{d\sigma}{d\epsilon\,d\Omega}\right\rangle_{\Delta\epsilon}\simeq\frac{1}{16\pi}\int_0^1 dq\frac{dS}{dq}I_{\Delta\epsilon}(2q(1-\cos\theta)-\epsilon). \tag{16}$$

This form indicates that spectra at different angles are scaled with a factor of $1-\cos\theta$, which is known for the peak position of a rotational rainbow [3]. Equation (16) exhibits the scaling when vibrational excitation is also taken into consideration.

C. Representation with orientation angle γ

The equipotential surface $\mathcal{S}_E$ is conveniently represented by a solution $r=r_S(x,R)$ of $E=V(r,x,R)$ with three scalar variables r, $x=\hat{\boldsymbol{r}}\cdot\hat{\boldsymbol{R}}$, and R. Since x represents the orientation angle ($\gamma=\cos^{-1}x$) at a contact position (s_1,s_2), the integral (12) over q is transformed into

$$\sigma_\xi=\int_{-1}^{1}dx\frac{dS}{dx}F_\xi(q(x)). \tag{17}$$

The integrand includes two functions of x, dS/dx and $q(x)$. They are expressed as

$$\frac{dS}{dx}=2\pi R_{\rm eq}^2u(x)\sqrt{u^2(x)+(1-x^2)u'^2(x)}, \tag{18}$$

$$q(x)=\frac{m}{M}u^2(x)\frac{v^2(x)+(1-x^2)u'^2(x)}{u^2(x)+(1-x^2)u'^2(x)}, \tag{19}$$

with $u(x)=r_S(x,R_{\rm eq})/R_{\rm eq}$ and $v(x)=[\partial r_S(x,R)/\partial R]_{R=R_{\rm eq}}$, using geometrical relations given in the Appendix. Hence, all the single- and double-differential cross sections (13)–(16), convoluted and unconvoluted, are analytically expressed in the form of Eqs. (17)–(19).

In particular, the unconvoluted energy-loss spectrum (14) is rewritten as

$$\frac{d\sigma}{d\epsilon d\Omega}=\frac{\sqrt{1-\epsilon}}{32\pi(1-\cos\theta\sqrt{1-\epsilon})}\times\sum_k\left[\frac{dS}{dx}[1+q(x)]^3\left|\frac{dq}{dx}\right|^{-1}\right]_{x=x_k(q^*)}, \tag{20}$$

where $q^*=q^*(\epsilon,\cos\theta)$ is given by Eq. (10), and $x_k(q^*)$ denotes a solution of $q(x)=q^*$ with k ($=1,2,\ldots$) labeling its branches. Note that summation over the branches k is taken in Eq. (20), whereas automatically incorporated in Eq. (15) for convoluted spectrum. Among three factors in the brackets of Eq. (20), dS/dx and $1+q(x)$ are regular and of small variation, whereas $|dq/dx|^{-1}$ may be singular. Thus, the spectral profile is primarily given by a factor $|dq/dx|^{-1}$; spectral features are induced by extrema of the inelasticity function $q(x)$. If $q(x)$ takes a local minimum or maximum at $x=x_R$, the spectrum has an integrable singularity at $q=q_R\equiv q(x_R)$ as

$$\left|\frac{dq}{dx}\right|^{-1}_{x=x_k(q)}\propto\frac{1}{\sqrt{q-q_R}}. \tag{21}$$

This singularity originates from an average over molecular orientations and gives rise to a peak feature in convoluted spectrum, hence analogous to the *rotational rainbow*. The rainbow of Eq. (21) refers, however, to the energy-loss spectrum with vibrotational states left unresolved, while the genuine rotational rainbow to the angular momentum j distribution in vibrationally elastic scatterings. In addition to a rainbow, the spectrum has a *step* feature at $q=q(\pm1)\equiv q_{\pm1}$ as

$$\left|\frac{dq}{dx}\right|^{-1}_{x=x_k(q)}\propto\vartheta(\mp q'(\pm1)(q-q_{\pm1})), \tag{22}$$

due to a contribution from the neighborhood of boundary points $x=\pm1$. If $|q'(\pm1)|\ll1$, however, the contribution around $q\simeq q_{\pm1}$ makes a peak, hence actually undistinguishable from a rainbow in convoluted spectra.

Inelasticity (19) is decomposed into rotational and vibrational contributions as $q=q_{\rm rot}+q_{\rm vib}$, where

$$q_{\rm rot}(x)\equiv\frac{m}{M}\left[\hat{\boldsymbol{R}}\times\frac{\partial s}{\partial\boldsymbol{R}}\right]^2_{s=0}=q(x)\frac{(1-x^2)u'^2(x)}{(1-x^2)u'^2(x)+v^2(x)}, \tag{23}$$

$$q_{\rm vib}(x)\equiv\frac{m}{M}\left[\hat{\boldsymbol{R}}\cdot\frac{\partial s}{\partial\boldsymbol{R}}\right]^2_{s=0}=q(x)\frac{v^2(x)}{(1-x^2)u'^2(x)+v^2(x)}. \tag{24}$$

Correspondingly, energy-loss is given by a sum of rotational and vibrational parts just after the collision as $\epsilon=\epsilon_{\rm rot}+\epsilon_{\rm vib}$, where $\epsilon_{\rm rot}=(\hat{\boldsymbol{R}}\times\delta\boldsymbol{P})^2/(2ME)$ and $\epsilon_{\rm vib}=(\hat{\boldsymbol{R}}\cdot\delta\boldsymbol{P})^2/(2ME)$. They are written as $\epsilon_{\rm rot}=[q_{\rm rot}/q]\epsilon$ and $\epsilon_{\rm vib}=[q_{\rm vib}/q]\epsilon$, irrespective of the scattering angle θ. Equations (23) and (24) indicate that $q_{\rm rot}$ and $q_{\rm vib}$ are, respectively, generated by partial derivatives $\partial r_S/\partial x\propto u'(x)$ and $\partial r_S/\partial R=v(x)$, relating to static and vibration-induced deformations of the surface $\mathcal{S}_E$. Thus, while the model applies to a vibrotator molecule with $q=q_{\rm vib}+q_{\rm rot}$, it is reduced to a rigid-rotor molecule by setting $q=q_{\rm rot}$ with dS/dx left unaltered, i.e., by setting $v(x)=0$ with $u(x)$ left unaltered in Eqs. (17)–(19); the hard potential model turns out to be a natural extension of the hard shell model (see Ref. [28]). We note, however, that the rotational energy-loss $\epsilon_{\rm rot}$ for a vibrotator does not coincide with that for a rigid-rotor because of nonlinearity of ϵ with q [see Eq. (11)].

A remark is added that the impulse given by Eq. (5) is shown to satisfy exactly the angular-momentum conservation $\boldsymbol{r}\times\delta\boldsymbol{p}+\boldsymbol{R}\times\delta\boldsymbol{P}=\boldsymbol{0}$, along with the energy conservation. This is an advantage of the present classical model.

III. SPECTRAL PROFILE FOR HOMONUCLEAR MOLECULE

As indicated in the preceding section, the energy-loss spectrum is primarily characterized by inelasticity function $q(x)$. In this section, we analyze extremum structures in $q(x)$ to show that the hard potential model generally gives a certain spectral profile for a homonuclear diatomic molecule; the spectrum has widely spaced double peaks, one nearly elastic and another deeply inelastic. Although evident for a

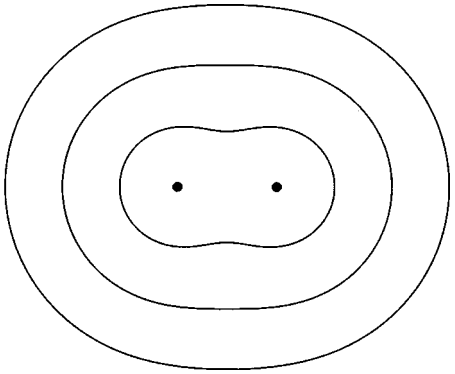

FIG. 3. Equipotential surfaces generated by an intermolecular potential in the form of Eq. (25) with a normalized range of $\lambda_0/R_{\rm eq}=0.25$ at three normalized strengths $V_0/E=10^3$, 10^2, and 10^1. The two closed circles indicate the equilibrium nuclear positions separating with a distance $R_{\rm eq}$ in the molecule.

rigid-rotor molecule, the emergence of double peaks is not obvious when vibrational excitation is taken into account.

The inelasticity function $q(x)$ is algebraically given in Eq. (19) by three quantities $u(x)$, $u'(x)$, and $v(x)$. Among them, $u(x)$ is calculated from a potential $V(r,x,R)$ by solving an equation $E=V(r,x,R)$ with $r=u(x)R_{\rm eq}$ and $R=R_{\rm eq}$. Then, $u'(x)$ and $v(x)$ are obtained from $u(x)$ through partial derivatives $u'(x)=-[\partial V/\partial x]/[R\partial V/\partial r]$ and $v(x)=-[\partial V/\partial R]/[\partial V/\partial r]$ at $r=u(x)R_{\rm eq}$ and $R=R_{\rm eq}$. The derivatives of $q(x)$ may be also calculated in algebra by using higher partial derivatives of $V(r,x,R)$. For a potential, the pairwise Born-Mayer form is conveniently assumed,

$$V(r,x,R)=V_{\rm AB}(\rho_-)+V_{\rm AC}(\rho_+), \tag{25}$$

where $\rho_\pm=\sqrt{r^2\pm xrR+R^2/4}$ and $V_{\rm AB}(\rho)=V_{\rm AC}(\rho)=V_0\exp(-\rho/\lambda_0)$. For this form, the equipotential surface $\mathcal{S}_E$ is characterized by two nondimensional parameters V_0/E (normalized potential strength) and $\lambda_0/R_{\rm eq}$ (normalized potential range), or equivalently by the normalized major and minor semiaxes of the surface, $a_\parallel\equiv u(\pm1)$ and $a_\perp\equiv u(0)$ (see Ref. [29]). As an illustration, the surfaces are plotted in Fig. 3 using the parameters as $\lambda_0/R_{\rm eq}=0.25$ with $V_0/E=10^3$, 10^2, and 10. It is seen in the figure that, as the strength decreases, the surface is shrinked in size and deformed in shape; it becomes slightly concave near the minor axis at $V_0/E=10$.

The hard potential model is expected to be valid when the force range is as short as

$$\exp(-R_{\rm eq}/\lambda_0)\equiv\eta\ll1, \tag{26}$$

and in addition when the surface $\mathcal{S}_E$ obtained is convex, i.e.,

$$a_\perp^2>\frac{\ln\eta}{32}[\ln\eta-\sqrt{(\ln\eta)^2+16}]. \tag{27}$$

Under such conditions, the spectrum behaves as illustrated in Fig. 4. In three panels are, respectively, plotted inelasticity function $q(x)$, spectral profile factor $|dq/dx|^{-1}$, and its convolution $\langle|dq/dx|^{-1}\rangle_{\Delta q}$ with a finite resolution Δq. The

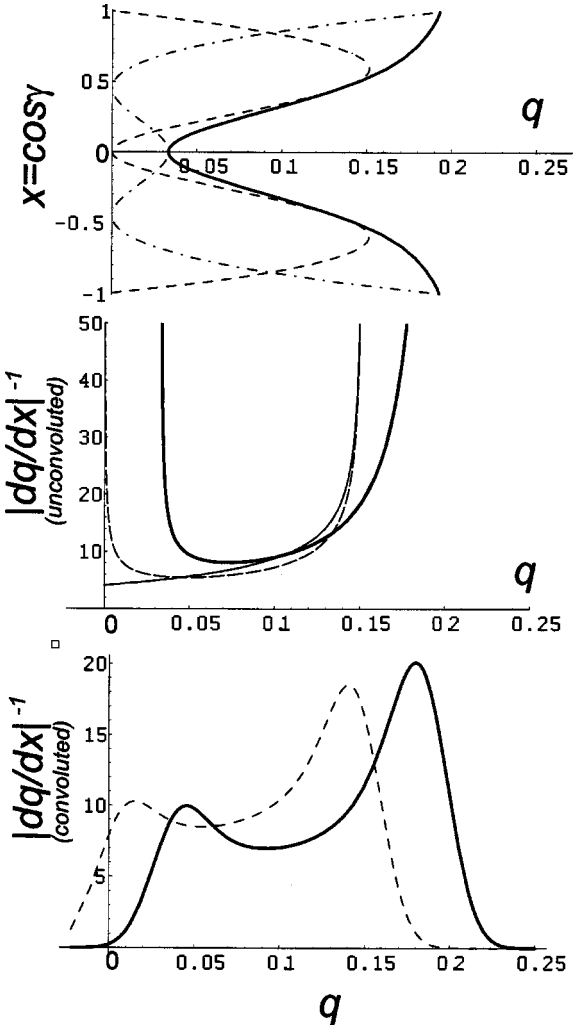

FIG. 4. The inelasticity functions $q(x)$ (upper panels), and the spectral profile factor $|dq/dx|^{-1}$ when unconvoluted (middle panels) and convoluted (lower panels). In the upper panels are shown the net $q(x)$ (solid lines) together with the separate contributions $q_{\rm rot}(x)$ (dashed lines) and $q_{\rm vib}(x)$ (dot-dash lines). In the middle and lower panels are plotted the spectra given by the net $q(x)$ (solid lines) and those only by $q_{\rm rot}(x)$ (dashed lines). The inelasticity functions are calculated using potential parameters of $\lambda_0/R_{\rm eq}=0.25$ and $V_0/E=10^2$ with a reduced-mass ratio of $m/M=0.8$. The convoluted spectra in the lower panel are obtained with a Gaussian instrumental function of a width (FWHM) $\Delta q=0.2\sqrt{\ln 2}m/(4M)$.

horizontal axes are taken in common to be the variable q; structures of energy-loss spectra are readily related to those of $q(x)$. We note here that approximately $\epsilon\propto q$ as far as $q\ll1$ [see Eq. (11)].

As seen in the upper panel, the inelasticity $q(x)$ takes a minimum at $x=0$ and maxima at boundary points $x=\pm1$ as

$$q_{\rm min}=q(0)=\frac{m}{16Ma_\perp^2}, \tag{28}$$

$$q_{\rm max}=q(\pm1)=\frac{m}{4M}\left(\frac{1-\eta}{1+\eta}\right)^2. \tag{29}$$

In this panel are also plotted the rotational $q_{\rm rot}(x)$ and vibrational $q_{\rm vib}(x)$ contributions. They exhibit out-of-phase oscillations with x. The $q_{\rm rot}(x)$ has maxima around $x \simeq \pm 0.6$ and vanishing minima at $x=0$ and $x=\pm 1$, while the $q_{\rm vib}(x)$ has vanishing minima around $x \simeq \pm 0.5$ and maxima at $x=0$ and $x=\pm 1$. In contrast to respective $q_{\rm rot}(x)$ and $q_{\rm vib}(x)$, however, the net $q(x)$ increases with $|x|$ in all the domain of $-1 \leqslant x \leqslant 1$. This behavior is generally confirmed because $[d^2q/dx^2]_{x=0} > 0$ and $\pm[dq/dx]_{x=\pm 1} > 0$; both relations are shown to be valid when Eqs. (26) and (27) are satisfied.

Corresponding to the behaviors of $q(x)$, the unconvoluted spectrum takes a profile as shown in the middle panel. The hard shell model ($q=q_{\rm rot}$) gives two branches; one has a step at $q=0$ [see Eq. (22)] and a rainbow at a maximum of $q_{\rm rot}$ [see Eq. (21)], and another has two rainbows at both edges (see Ref. [30]). The step structure in the former branch is veiled by the rainbow in the latter branch. On the other hand, the hard potential model ($q=q_{\rm rot}+q_{\rm vib}$) has a single curve accompanied by two distinct rises at both edges of the spectrum. The structure at $q_{\rm min}$ is a rainbow divergence [$q'(0)=0$]. The structure at $q_{\rm max}$ exactly makes a step ($q'(\pm 1) \neq 0$), but it tends to a rainbow as $\eta \to 0$ [see Eq. (26)] because $q'(\pm 1) = O(\eta \ln \eta)$.

After convolution, however, the two models give similar spectral profiles as seen in the lower panel; the spectra have widely spaced double peaks at $q \simeq q_{\rm min}$ and $q_{\rm max}$, irrespective of a rainbow [see Eq. (21)] or a step [see Eq. (22)] before convolution. The effect of vibrational excitation manifests itself in a shift of peak positions towards larger q, with peak heights left almost unaltered. The hard potential model derives a spectral domain in larger energy-losses than the hard shell model. The minimum position $q_{\rm min}$ increases with decreasing minor axis $a_\perp$ [see Eq. (28)]. The maximum position $q_{\rm max}$ is determined almost exclusively by a reduced-mass ratio m/M [see Eqs. (26) and (29)].

IV. COMPARISON WITH CLASSICAL TRAJECTORY CALCULATIONS

As formulated in Sec. II, the hard potential model is given in the limit $\lambda \to 0$ of a vanishing range of force, though it is not realistic in principle. In this section, we calculate classical trajectories with a realistic potential of finite λ, and systematically compare them with the model. We demonstrate how the model works and how the effects of finite λ manifest themselves in the energy-loss spectra.

The coupled Newton equations of motion are derived from the Hamiltonian of Eq. (1) for a vibrotator molecule, and numerically solved with the Verlet's algorithm [31]. This procedure is also applied for a rigid-rotor molecule using the method of Lagrange multiplier [32]. Cross sections are obtained on the basis of Eqs. (2) and (3) from a plenty ($\sim 10^5$) of trajectories with initial conditions assumed below Eq. (1). We investigate single- and double-differential cross sections. Analysis of the former supports that of the latter.

The calculations are carried out for collision systems of $H^+ + N_2$ and of $^7Li^+ + N_2$. For the two systems, we assume common effective interaction and set a common center-of-mass energy as $E=1$ (atomic units are used in this section); a difference only comes from the reduced mass m ($m/M = 0.14$ for $H^+ + N_2$ and $m/M = 0.80$ for $^7Li^+ + N_2$). Interaction potentials are taken to be the same that Gierz *et al.* [21] used for the analysis of measured spectra in $^7Li^+ + N_2$ collisions at $E=0.62$. The intermolecular potential is given in the pairwise form of Eq. (25) with parameters of $V_0 = 1.3 \times 10^2$, $\lambda_0 = 0.50$, and $R_{\rm eq} = 2.1$. The intramolecular potential is given in the Morse form as $U(r) = U_0\{\exp[-2(R - R_{\rm eq})/\beta_0] - 2\exp[-(R-R_{\rm eq})/\beta_0]\}$ with $U_0 = 0.36$ and $\beta_0 = 0.70$.

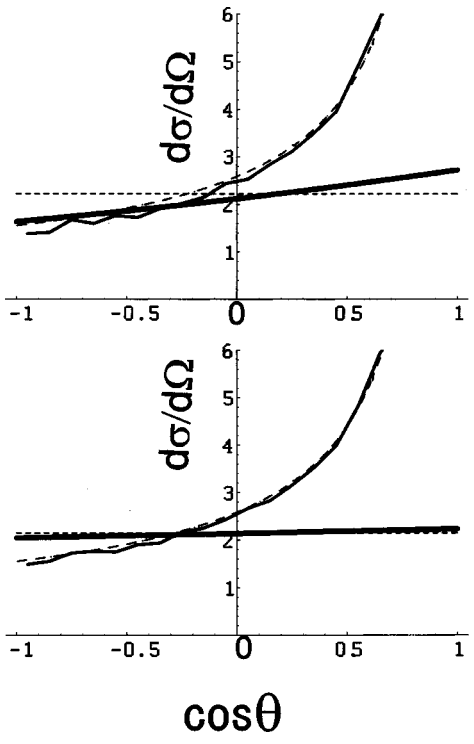

FIG. 5. Differential cross sections $d\sigma/d\Omega$ at $E=1$ a.u. for collision systems of $H^+ + N_2$ (the lower panel) and $^7Li^+ + N_2$ (the upper panel). Plotted are the results of the vibrotator CT calculations (thin solid lines) and of the hard potential model (thick solid lines), together with scatterings by a diffuse potential $V_{\rm sph}(r)$ (dashed lines) and by a rigid sphere (dotted lines).

A. Single-differential cross section

Results of the vibrotator CT calculation are shown in Fig. 5 for the angular distribution $d\sigma/d\Omega$ and compared with the hard potential model.

As seen in the figure, the model gives almost linear dependence on $\cos\theta$. According to Eq. (13), they are written as $d\sigma/d\Omega \simeq (a^2/4)[1 + 2\langle q \rangle \cos\theta]$, with an effective radius a and a mean inelasticity $\langle q \rangle$ over the equipotential surface $\mathcal{S}_E$. The radius is determined so as to reproduce the total area of $\mathcal{S}_E$ as $\int dS = 4\pi a^2$, and calculated to be $a=3.0$ in the present case. Angular dependence comes, through $\langle q \rangle$, from excitations of molecular internal freedoms. The slope is appreciable in $Li^+ + N_2$, whereas negligible in $H^+ + N_2$, because inelasticity q is proportional to mass ratio m/M [see Eq. (8)].

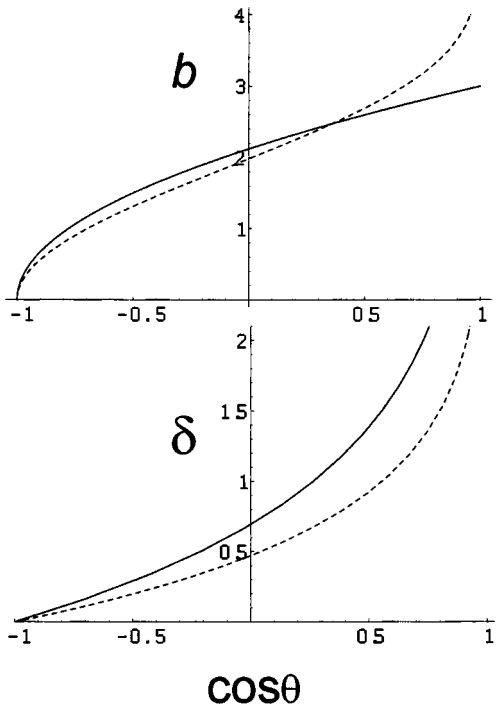

FIG. 6. The deflection function (the upper panel) and the distance r_{ca} of the closest approach (the lower panel) at $E=1$ a.u. generated by a spherical potential $V_{sph}(r)=E\exp[-(r-a)/\lambda]$ with $a=3.0$. They are plotted when $\lambda=0.5$ (dashed lines) and when $\lambda=0$ (solid lines). The deflection function is represented as impact parameter b vs $\cos\theta$, while the closest approach as $\delta=(r_{ca}-a)/\lambda$ vs $\cos\theta$.

On the other hand, the CT calculation exhibits nonlinear dependence on $\cos\theta$, which diverges as $\cos\theta\to1$. In backward angles ($\cos\theta<0$), however, it shows moderate agreement with the model, better in $Li^+ + N_2$ than in $H^+ + N_2$. The angular distributions are also compared in the figure with those given by a spherical potential $V_{sph}(r)=E\exp[-(r-a)/\lambda]$ with a diffuseness of $\lambda=0.50$, the same value as in the pairwise intermolecular potential taken above. They show good accordance with the result of CT calculation, except at backward angles for $Li^+ + N_2$. This observation indicates that the nonlinear dependence primarily stems from distortion of trajectories due to a diffuse potential, which virtually masks internal excitation in $H^+ + N_2$. Thus, the two effects are discernible; for a given energy E, trajectory distortion is independent of the reduced mass m, while internal excitation crucially depends on m.

We note that internal excitation itself may be perturbed by trajectory distortion during a collision. To make a guess, we show in Fig. 6 the deflection function θ (of the impact parameter b) and the distance r_{ca} of closest approach using the diffuse potential $V_{sph}(r)$ above. Correlating to each other, the θ and r_{ca} are seen to deviate from behaviors of the rigid sphere conspicuously at forward angles. Unless $\cos\theta>0.5$, however, the deflection function is reasonably reproduced by the rigid sphere. In addition, the distance r_{ca} is close to the radius a in such a degree as $|r_{ca}-a|<\lambda\ll a$. On this basis, we expect the hard potential model to be valid for scattering angles larger than about 60°.

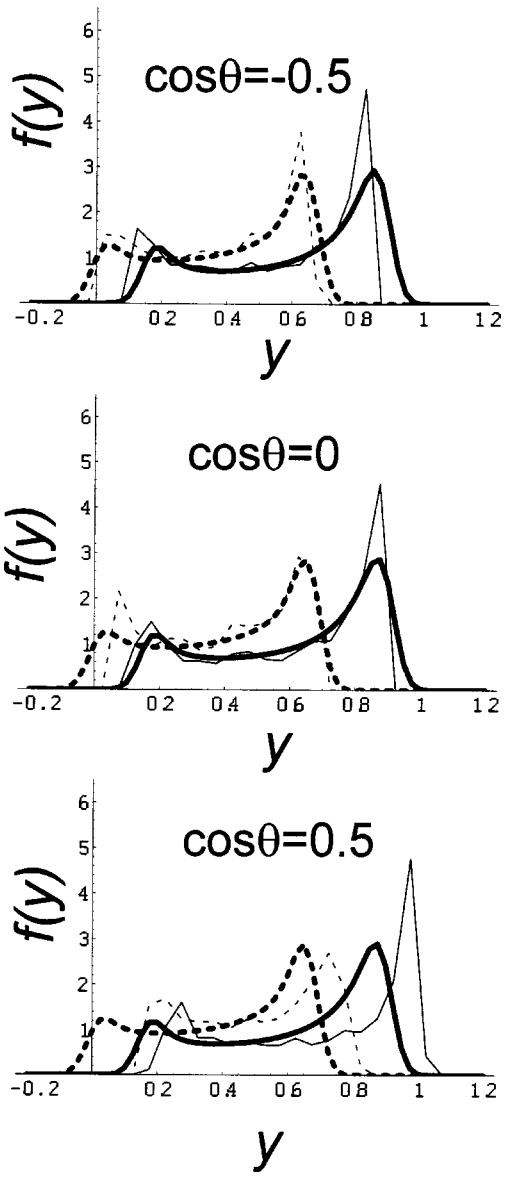

FIG. 7. The scaled energy-loss spectra $f(y)$ [see Eq. (30)] at three scattering angles of $\cos\theta=-0.5$, 0, and 0.5 for a mass ratio of $m/M=0.14$ (corresponding to $H^+ + N_2$). Results of four methods are plotted: the hard shell model (thick dashed lines), the hard potential model (thick solid lines), the rigid-rotor CT calculation (thin dashed lines), and the vibrotator CT calculation (thin solid lines).

B. Double-differential cross section

Energy-loss spectra $d\sigma/(d\epsilon\, d\Omega)$ are calculated at three scattering angles of $\cos\theta=-0.5$, 0, and 0.5, and shown in Figs. 7 and 8, respectively, for $Li^+ + N_2$ and for $H^+ + N_2$. For convenience of comparison among different angles θ and different mass ratios m/M (i.e., the two systems), the energy-loss is scaled in the figures by a variable y such that

$$\epsilon=\frac{m}{M}\frac{1-\cos\theta}{2}y. \tag{30}$$

At each angle in each system are compared four methods, i.e., the rigid-rotor CT calculation, and the vibrotator CT

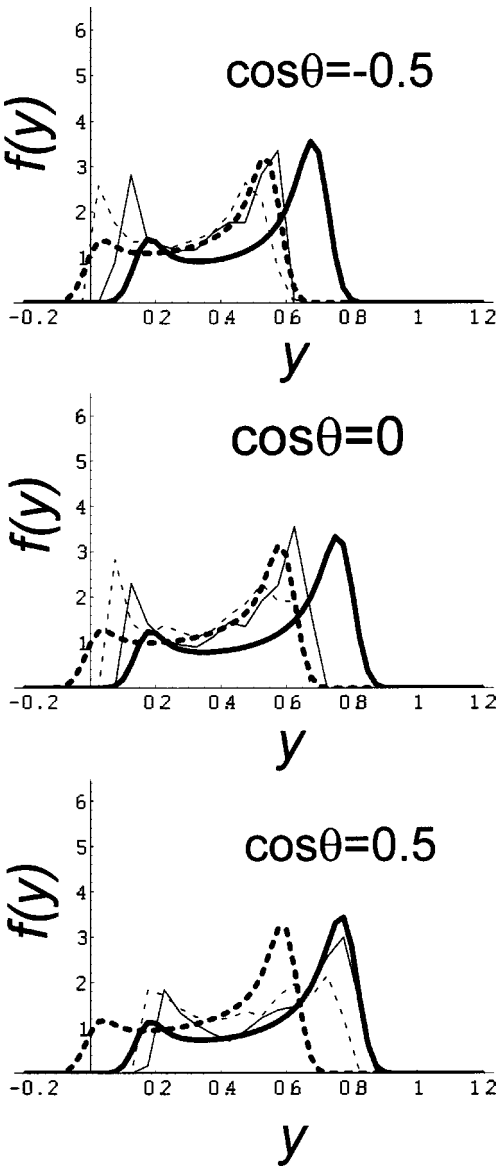

FIG. 8. The same as Fig. 7 except that the mass ratio is taken to be $m/M=0.80$ (corresponding to $Li^+ + N_2$).

calculation, the hard shell model, and the hard potential model. In the CT calculations, the trajectories are ''boxed'' with acceptance widths of $\Delta y=0.05$ and $\Delta\cos\theta=0.1$. In the models, the spectra are calculated using Eqs. (15), (18), and (19), and convoluted with a Gaussian instrumental function of a width [full width of half maximum (FWHM)] of $\Delta y = 0.2\sqrt{\ln 2}$. The spectra shown are, respectively, normalized in the four methods, as $\int f(y)dy=1$ where $f(y) \propto d\sigma/(d\epsilon\, d\Omega)$.

1. Predictions of the hard potential model and the hard shell model

Throughout Figs. 7 and 8, both the models give spectral profiles with widely spaced double peaks. The spectra shown are almost identical at different angles and mass ratios when scaled by the variable y; its domain is almost restricted as $0<y<1$. In fact, Eqs. (8), (16), and (30) indicate a scaling relation with y if $q \ll 1$ all over the equipotential surface $\mathcal{S}_E$. When such is the case, the variable y is determined only by the surface $\mathcal{S}_E$ as $y \simeq |\partial s/\partial \boldsymbol{R}|^2$ in hard potential model [see Eq. (8)], or as $y \simeq |\hat{\boldsymbol{R}} \times (\partial s/\partial \boldsymbol{R})|^2$ in the hard shell model [see Eq. (23)]. The difference in y between the two models is caused by vibrational excitation. The double peaks shown are thereby shifted in parallel towards larger energy-losses by about 0.2 in variable y, while the peak heights are little altered. In particular, the nearly elastic peak emerges at $y \simeq 0$ in the hard shell model, while at $y \simeq 0.2$ in the hard potential model.

TABLE I. Vibrational suddenness $\omega_{\rm vib}\tau$ and corresponding parameter β of the Morse potential employed for the vibrotator CT calculation in Figs. 9 and 10.

	$\omega_{\rm vib}\tau$	β for $H^+ + N_2$	β for $Li^+ + N_2$
Case (a)	0.12	1.69	4.07
Case (b)	0.30	0.70 ($=\beta_0$)	1.69
Case (c)	0.73	0.29	0.70 ($=\beta_0$)
Case (d)	1.78	0.12	0.29

Small variation with angles and systems is seen, however, in a position of the deeply inelastic peak. The hard potential model derives the peak for $H^+ + N_2$ at $y=0.84$–0.87, while for $Li^+ + N_2$ at smaller y as 0.63–0.76 slightly increasing with $\cos\theta$. Similarly, the hard shell model derives the peak at $y=0.63$–0.65 for $H^+ + N_2$, while at $y=0.50$–0.58 for $Li^+ + N_2$. These dependences indicate a departure from the y scaling with increasing m/M and $1-\cos\theta$ as a nonlinear effect with inelasticity q [see Eq. (11)].

2. Comparison of rigid-rotor CT calculation with the hard shell model

Throughout Figs. 7 and 8, the rigid-rotor CT calculation derives a gross profile of double peaks; overall spectra follow the hard shell model fairly well. This observation is associated with the sudden character of rotational excitation. Its criterion is given by a phase change $\omega_{\rm rot}\tau \ll 1$ with rotational angular frequency $\omega_{\rm rot}$ in collision time τ, while the hard shell model represents the sudden limit $\omega_{\rm rot}\tau \to 0$ because $\tau \propto \lambda \to 0$. The change is estimated [15] to be $\omega_{\rm rot}\tau \simeq (m/M)(\lambda_0/R_{\rm eq})(a_\parallel - a_\perp) = 0.015$ in $H^+ + N_2$, and 0.10 in $Li^+ + N_2$. Hence, although the latter is less perfect, both systems are considered to be sudden.

For the peak positions, however, small but systematic departures from the model are found. At backward angles ($\cos\theta=-0.5$ and 0), the deeply inelastic peak is appreciably shifted towards smaller y in $Li^+ + N_2$, in contrast to $H^+ + N_2$. This behavior is explainable as due to imperfect suddenness mentioned above; the sudden limit accounts for an upper bound of the energy-loss. At a forward angle ($\cos\theta = 0.5$), the double peaks are considerably shifted in parallel towards larger y. This behavior is common in the two systems, hence interpreted as coming from trajectory distortion by a diffuse potential as shown in Fig. 6. The deeply inelastic

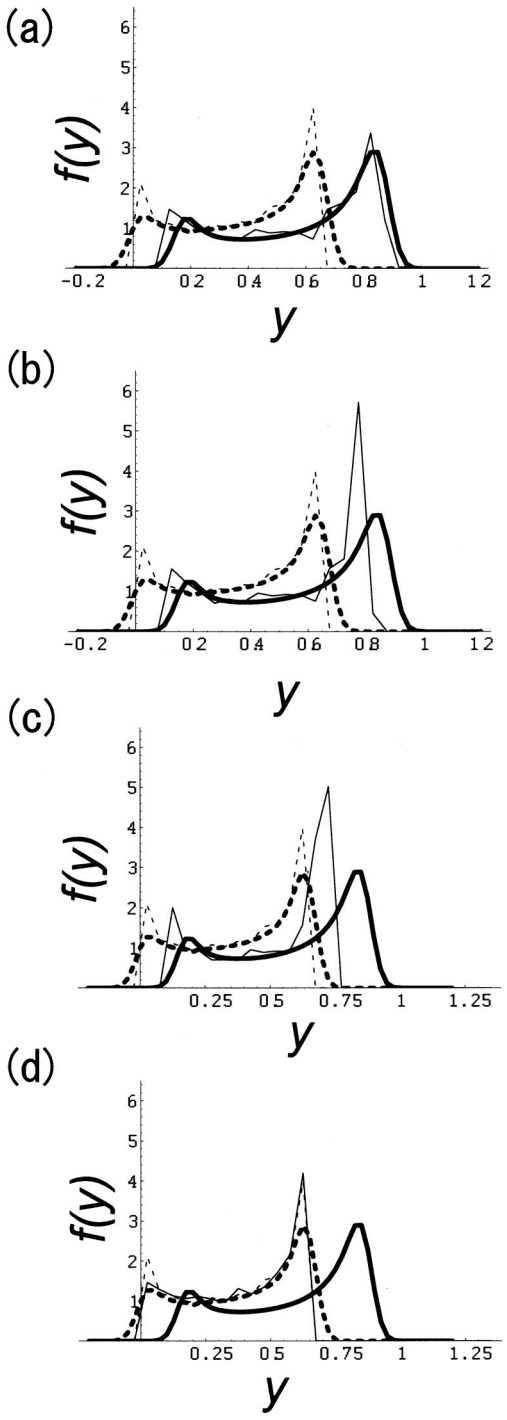

FIG. 9. The scaled energy-loss spectra $f(y)$ [see Eq. (30)] at a scattering angle of $\cos\theta=-1$ for a mass ratio of $m/M=0.14$ (corresponding to $H^+ + N_2$). Results of four methods are plotted in the same way as in Fig. 7. In four panels (a)–(d), the vibrational period is, respectively, modified according to cases (a)–(d) in Table I. The vibrotator CT calculation depends on them, though the other three methods give common spectra among the four panels.

peak could be contributed from those trajectories which would be deflected into larger angles by a hard potential. The nearly elastic peak may be contributed from an extended region of interaction.

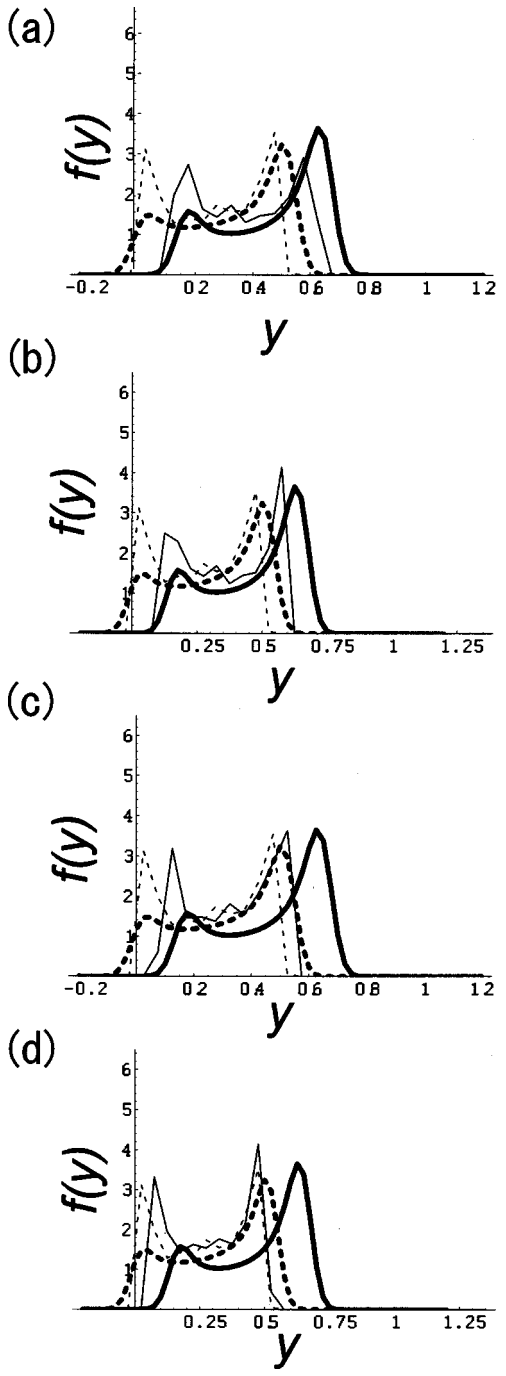

FIG. 10. The same as Fig. 9 except that the mass ratio is taken to be $m/M=0.80$ (corresponding to $Li^+ + N_2$).

3. Analyses of vibrotator CT calculation with the models

Throughout Figs. 7 and 8, the vibrotator CT calculation derives an overall profile of double peaks. The spectral domain is shifted towards larger y with $\cos\theta$, which is associated primarily with trajectory distortion by a diffuse potential. These behaviors are analogous to those found above in the rigid-rotor CT calculation. However, the double peaks are located at larger energy-losses, reflecting the effect of vibrational excitation.

At backward angles ($\cos\theta=-0.5$ and 0), the vibrational effect is found to be considerably larger in $H^+ + N_2$ than in

$Li^+ + N_2$. The deeply inelastic peak is nearly reproduced by the hard potential model in $H^+ + N_2$, while rather by the hard shell model in $Li^+ + N_2$. These observations are associated with the sudden character of vibrational excitation. Its criterion is given by a phase change $\omega_{\rm vib}\tau \ll 1$ with vibrational angular frequency $\omega_{\rm vib}$ in collision time τ. The change is estimated to be $\omega_{\rm vib}\tau \simeq (2\lambda_0/\beta_0)\sqrt{U_0/E}\sqrt{m/M} = 0.30$ for $H^+ + N_2$, and 0.73 for $Li^+ + N_2$. Hence, larger vibrational excitation found in the former system is explainable as better suddeness due to smaller mass m.

To further elucidate the sudden character, we make CT calculations by artificially modifying the Morse potential as $\beta_0 \to \beta$. With this procedure, we can adjust vibrational suddenness, while conserving rotational suddenness along with the equipotential surface $\mathcal{S}_E$. Four different cases (a)–(d) are considered according to Table I. The realistic value β_0 is included in (b) for $H^+ + N_2$, and in (c) for $Li^+ + N_2$. The condition of $\omega_{\rm vib}\tau \ll 1$ is duly satisfied in (a), but no more in (d). Thus, comparison among the four cases resolves the degree of vibrational suddenness when rotational excitation is almost sudden.

The results at $\cos\theta = 1$ are shown in Figs. 9 and 10, respectively, for $H^+ + N_2$ and $Li^+ + N_2$. In $H^+ + N_2$, the peak shift between vibrotator and rigid-rotor CT calculations is largest in case (a), decreasing with $\omega_{\rm vib}\tau$, and negligible in case (d). In case (a), the overall spectrum is well reproduced by the hard potential model, which represents the sudden limit for both rotational and vibrational excitations, $\omega_{\rm rot}\tau \to 0$ and $\omega_{\rm vib}\tau \to 0$, because $\tau \propto \lambda \to 0$. In case (d), the vibrotator spectrum is reduced to the rigid-rotor one, hence well reproduced by the hard shell model; vibrational motion is virtually adiabatic and hardly excited. The parallel behaviors are also found in $Li^+ + N_2$, though the effect of imperfect rotational suddenness is appreciable.

V. CONCLUDING REMARKS

In the present paper, we have developed the hard potential model for collisions of an atom (or an ion) with a diatomic molecule by taking the limit of a vanishing range of force. The model has an ideally sudden character for both vibrational and rotational excitations, in the same way as the hard shell model for purely rotational excitation [9]. The energy-loss spectrum is described by the inelasticity function $q(x)$ defined on the equipotential surface, which turns out to be an extension of the hard shell model developed by Beck *et al.* [7,11]. For a homonuclear molecule, an overall spectral profile with double peaks is derived, almost independent of the scattering angle and the reduced mass. The effect of vibrational excitation manifests itself in a shift of the peak positions (by 20–30 %).

The CT calculations using a finite-range model potential have been carried out for collisions of $H^+ + N_2$ and of $Li^+ + N_2$ at $E = 1$ a.u. The calculations have confirmed the effect of vibrational excitation the way the model predicts. It is also demonstrated that the spectra are virtually reduced to the hard potential model when the vibrational period is artificially taken much longer than a collision time, while reduced to the hard shell model when much shorter.

Thus, the hard potential model serves as a standard for revealing systematic effects of vibrational excitation in the energy-loss spectra. Analyses of experimental spectra with this model will be promising.

ACKNOWLEDGMENTS

We are grateful to Professor S. Kita, Professor H. Tanuma, and Professor Y. Itikawa for valuable discussions. We would like to express our sincere thanks to Professor K. Takayanagi for his comments in the early stages of this work.

APPENDIX: REPRESENTATION OF VECTORS $\partial S/\partial R$ AND $\partial S/\partial R$

The solution $r = r_S(x,R)$ of $E = V(r,x,R)$ is also a solution of $0 = s(r,x,R)$, thus satisfying $\partial r_S/\partial x = -[(\partial s/\partial x)/(\partial s/\partial r)]_{s=0}$ and $\partial r_S/\partial R = -[(\partial s/\partial R)/(\partial s/\partial r)]_{s=0}$. Hence, by noting that $\partial s/\partial r = \hat{\boldsymbol{r}}\cdot\hat{\boldsymbol{n}}$ with normal vector $\hat{\boldsymbol{n}} = \partial s/\partial \boldsymbol{r}$, we can write

$$\left.\frac{\partial s}{\partial \boldsymbol{r}}\right|_{s=0} = \hat{\boldsymbol{r}}\cdot\hat{\boldsymbol{n}}\left(\hat{\boldsymbol{r}} + \frac{\sqrt{1-x^2}}{r_S(x,R)}\frac{\partial r_S}{\partial x}\hat{\boldsymbol{t}}\right)_{R=R_{\rm eq}},$$

$$\left.\frac{\partial s}{\partial \boldsymbol{R}}\right|_{s=0} = \hat{\boldsymbol{r}}\cdot\hat{\boldsymbol{n}}\left(-\frac{\partial r_S}{\partial R}\hat{\boldsymbol{R}} + \frac{\sqrt{1-x^2}}{R}\frac{\partial r_S}{\partial x}\hat{\boldsymbol{T}}\right)_{R=R_{\rm eq}},$$

with two unit vectors $\hat{\boldsymbol{t}} \equiv (x\hat{\boldsymbol{r}} - \hat{\boldsymbol{R}})/\sqrt{1-x^2}$ and $\hat{\boldsymbol{T}} \equiv (x\hat{\boldsymbol{R}} - \hat{\boldsymbol{r}})/\sqrt{1-x^2}$, where $\hat{\boldsymbol{t}}\cdot\hat{\boldsymbol{r}} = 0$ and $\hat{\boldsymbol{T}}\cdot\hat{\boldsymbol{R}} = 0$.

[1] A.S. Dickinson and D. Richards, Adv. At. Mol. Phys. **18**, 165 (1982).
[2] M. Faubel, Adv. At. Mol. Phys. **19**, 345 (1983).
[3] R. Schinke and J. M. Bowman, in *Molecular Collision Dynamics*, edited by J. M. Bowman (Springer, Berlin, 1983), Chap. 3.
[4] H.J. Korsch and A. Ernesti, J. Phys. B **25**, 3565 (1992).
[5] J. P. Toennies, in *Semiclassical Descriptions of Atomic and Nuclear Collisions*, edited by J. Bang and J. de Boer (Elsevier Science, Amsterdam, 1985), p. 29.
[6] E. A. Mason and E. W. McDaniel, *Transport Properties of Ions in Gases* (Wiley, New York, 1988), Chap. 7.
[7] D. Beck, U. Ross, and W. Schepper, Z. Phys. A **293**, 107 (1979); **299**, 97 (1981).
[8] U. Ross, W. Schepper, and D. Beck, Chem. Phys. **61**, 95 (1981); U. Ross *et al.*, Z. Phys. A **320**, 25 (1985); D. Beck, in *Physics of Electronic and Atomic Collisions*, edited by S. Datz (North-Holland, Amsterdam, 1982), p. 331.
[9] U. Buck, Comments At. Mol. Phys. **17**, 143 (1986); U. Buck *et al.*, J. Chem. Phys. **82**, 202 (1985).
[10] D. Beck, Chem. Phys. **126**, 19 (1988).

[11] M. Velegrakis and D. Beck, J. Chem. Phys. **94**, 7981 (1991).
[12] S. Bosanac, Phys. Rev. A **22**, 2617 (1980); **26**, 282 (1982); **26**, 816 (1982); S. Bosanac and U. Buck, Chem. Phys. Lett. **81**, 315 (1981).
[13] M.H. Alexander and P.J. Dagdigian, J. Chem. Phys. **73**, 1233 (1980).
[14] J.A. Serri, R.M. Bilotta, and D.E. Pritchard, J. Chem. Phys. **77**, 2940 (1982).
[15] M. Nakamura, J. Phys. Soc. Jpn. **56**, 3145 (1987).
[16] A.J. McCaffery, Z.T. Alwahabi, M.A. Osborne, and C.J. Williams, J. Chem. Phys. **98**, 4586 (1993); A.J. McCaffery and R.J. Marsh, J. Phys. B **34**, R131 (2001).
[17] A.J. Marks, J. Chem. Soc., Faraday Trans. **90**, 2857 (1994).
[18] P.M. Agrawal, S. Tilwanker, and N.K. Dabkara, J. Chem. Phys. **108**, 4854 (1998).
[19] H. Kohguchi and T. Suzuki, Annu. Rep. Prog. Chem., Sect. C: Phys. Chem. **98**, 421 (2002).
[20] R. Boettner, U. Ross, and J.P. Toennies, J. Chem. Phys. **65**, 733 (1976).
[21] U. Gierz, J.P. Toennies, and M. Wilde, Chem. Phys. **2**, 115 (1984).
[22] S. Kita, H. Tanuma, I. Kusunoki, Y. Sato, and N. Shimakura, Phys. Rev. A **42**, 367 (1990).
[23] T. Hasegawa, S. Kita, M. Izawa, and H. Inouye, J. Phys. B **18**, 3775 (1985); M. Nakamura, S. Kita, and T. Hasegawa, J. Phys. Soc. Jpn. **56**, 3161 (1987); H. Tanuma, S. Kita, I. Kusunoki, and N. Shimakura, Phys. Rev. A **38**, 5053 (1988).
[24] E. Vilallonga and D.A. Micha, J. Chem. Phys. **84**, 3162 (1986); **86**, 750 (1987); **86**, 760 (1987).
[25] R.D. Sharma, P.M. Bakshi, and J.M. Sindoni, Phys. Rev. A **43**, 189 (1991); H. Dothe and R.D. Sharma, J. Chem. Phys. **98**, 4567 (1993).
[26] This result may be interpreted as elastic reflection from a fixed *hard wall* in a *six-dimensional* space. If we take canonical variables as $\vec{p} \equiv (\vec{p}, \sqrt{m/M}\vec{P})$ and $\vec{r} \equiv (\vec{r}, \sqrt{M/m}\vec{R})$, the present Hamiltonian reads as $H(\vec{p},\vec{r}) = \vec{p}^2/(2m) + V(\vec{r})$, where $V(\vec{r}) = +\infty$ for $s(\vec{r}) < 0$ and $= 0$ for $s(\vec{r}) > 0$ in the limit of $\lambda \to 0$. Hence, the six-dimensional impulse is given by twice the projection of incident momentum onto the normal vector to the hard wall surface $[s(\vec{r}) = 0]$. This leads to Eq. (6).
[27] In general, the impulse (6) can be exerted more than once in a collision. For such not being the case, we assume that the shape of the equipotential surface $\mathcal{S}_E$ is convex. Even then, multiple impulses are still possible because the potential $U(R)$ affects intramolecular motion after the first impulse, which may happen to lead to a configuration where the hard potential (5) works again. However, this is improbable if the incident atom *A* is much lighter than the constituent atoms *B* and *C* of the molecule.
[28] In fact, Eq. (23) is shown to be equivalent to a function "*B*" introduced in Ref. [11], with which Beck [7,11] derived the hard shell model by considering the force normal to the surface.
[29] They are expressed as $a_{\parallel} = (\lambda_0/R_{\rm eq})\ln[(2V_0/E)\cosh(R_{\rm eq}/\lambda_0/2)]$ and $a_{\perp} = \sqrt{[(\lambda_0/R_{\rm eq})\ln(2V_0/E)]^2 - 1/4}$.
[30] In usual terminology, "rotational rainbow" only refers to a divergence at the maximum of q, but not at $q = 0$. The latter divergence is absorbed in the Jacobian $dj/d\epsilon \propto 1/\sqrt{\epsilon}$, between the energy-loss ϵ and the angular momentum j in the hard shell model, so that the j distribution $d\sigma/(dj\, d\Omega)$ is finite at $j = 0$.
[31] L. Verlet, Phys. Rev. **159**, 98 (1967).
[32] R.A. La Budde and R.B. Bernstein, J. Chem. Phys. **55**, 5499 (1971); H. Goldstein, *Classical Mechanics* (Addison-Wesley, Reading, MA, 1950), Chap. 2.